RSC Advances

REVIEW

View Article Online
View Journal | View Issue

Check for updates

Cite this: *RSC Adv.*, 2020, **10**, 26742

Tumor microenvironment triggered biodegradation of inorganic nanoparticles for enhanced tumor theranostics

Weitao Yang,[a] Suhong Yang,*[b] Liping Jiang,[c] Yujuan Zhou,[b] Cuiling Yang[b] and Cuijun Deng *[a]

Received 26th May 2020
Accepted 10th July 2020

DOI: 10.1039/d0ra04651e

rsc.li/rsc-advances

Inorganic nanoparticles (NPs)-mediated tumor theranostics have attracted widespread attention due to their unique physicochemical properties, such as optical, electrical, magnetic, and thermal properties. In the past decade, great advancements have been made in inorganic NPs-associated drug delivery, multimodal tumor imaging, and tumor therapy. However, the potential toxicity of inorganic NPs due to their low biodegradability, background signals interference and treatment side effects limit their clinical application. Therefore, developing biodegradable and intelligent NPs is beneficial to avoid excessive metal ions deposition, specific tumor imaging and treatment. In this review, we summarize the recent advances in tumor microenvironment (TME)-triggered biodegradation of inorganic NPs accompanied by imaging signal amplification and the released ions-mediated tumor therapy. First, the feature characteristics of the TME are introduced, including mild acidity, hypoxia, overexpressed reactive oxygen species (ROS), glutathione (GSH), and enzymes *et al.*; then, the biodegradation of NPs in a TME-induced activation of imaging signals, such as magnetic resonance (MR) imaging and fluorescence imaging is described; furthermore, tumor therapies through "Fenton", "Fenton-like" reactions, and interference of biological effects in cells is presented. Finally, the challenges and outlook for improving the degradation efficiency, imaging, specificity and efficiency of tumor imaging and treatment are discussed.

1. Introduction

Malignant tumors are one of the most severe threats to human health, and the incidence and mortality remain very high worldwide.[1,2] In recent decades, the advent of nanotechnology has provided new opportunities for tumor theranostics due to the unique nanoeffect of nanoparticles (NPs). Among of which, inorganic NPs have been the subject of great attention based on their good stability and excellent physicochemical properties in many areas, including light, heat, sound, electricity, and magnetism *et al.* Compared with organic NPs, inorganic NPs exhibit more stable properties and can be reused multiple times. Moreover, these properties can be converted each other, which enrich the use of inorganic NPs.

To date, a series of inorganic NPs have been well known to be applied for tumor imaging and therapeutic research. For instance, metal nanoclusters,[3] quantum dots (QDs),[4] upconversion NPs (UCNPs),[5] and persistent luminescence NPs[6,7] have been proven to have significant antiphotobleaching properties in terms of cell fluorescent labeling and *in vivo* tumor fluorescence imaging. Gadolinium oxide and iron oxide are recognized as classic contrast agents (CAs) for magnetic resonance (MR) imaging;[8,9] Nanoparticles containing heavy metal elements (Au, Bi, Pt, and Hf) were usually used as computerized tomography (CT) imaging CAs depending on the strong attenuation of X-rays.[10,11] Metal sulfides, such as CuS and Bi_2S_3, can effectively and repeatedly convert the absorbed near-infrared (NIR) light into heat, which can be used for photothermal treatment and photoacoustic (PA) imaging of tumors;[12,13] Inorganic photosensitizers or sonosensitizers, such as TiO_2, $Au_{25}(Capt)_{18}$ nanoclusters, and $PtCu_3$ NPs can inhibit tumor growth by producing reactive oxygen species (ROS) under laser or ultrasonic excitation;[14–16] in particular, inorganic NPs with multimodal imaging and therapeutic functions have been continuously developed for precise tumor theranostics. For instance, our group synthesized Gd:CuS@BSA NPs by using an albumin-mediated biomimetic strategy. The obtained Gd:CuS@BSA NPs exhibited significant absorbance in NIR with high photothermal conversion efficacy (32.3%) and a significant longitudinal relaxation rate (r_1 = 16.032 mM^{-1} s^{-1}) than the clinical MR contrast agent

---

[a] Department of Medical Ultrasound, Shanghai Tenth People's Hospital, Ultrasound Research and Education Institute, Tongji University Cancer Center, Shanghai Engineering Research Center of Ultrasound Diagnosis and Treatment, Tongji University School of Medicine, Shanghai, 200072, China. E-mail: dcj_2014@126.com

[b] Department of Respiratory and Intensive Care Unit, Anqiu People's Hospital, Weifang, 262100, China. E-mail: ywttju@126.com

[c] State Key Laboratory of Molecular Engineering of Polymers, Department of Macromolecular Science, Fudan University, Shanghai, China, 200438

(Magnevist, $r_1 = 3.843\ \text{mM}^{-1}\ \text{s}^{-1}$). Thus, they were applied for *in vivo* tumor MR/PA imaging-guided photothermal therapy.[17] Overall, inorganic NPs demonstrate their versatility and excellent properties in tumor diagnosis and treatment. However, there are still some problems that need to be resolved: (1) compared with organic NPs, *in vivo* degradability and toxicity of inorganic nanoparticles have been a concern for a long time. After intravenous injection, inorganic NPs accumulate in tumors as well as normal tissues, and long-term deposition often produces toxicity, which limits its clinical application.[18] Therefore, degradability will become the primary consideration when synthesizing inorganic NPs in the future; (2) currently, most obtained inorganic NPs employ an "always-on" mode for tumor theranostics, which brings about some advantages. For tumor imaging, the "always-on" signal can produce strong background interferences *in vivo* and significantly reduce the signal-to-noise ratio (SNR) in the tumor site, hindering diagnostic efficiency.[19,20] For tumor therapy, if laser or ultrasonic treatments accidentally irradiate normal tissues, the inorganic NPs can also produce ROS or heat and cause notable side effects.

Considering the significantly different characteristics between the TME and normal tissues, such as mild acidity, hypoxia, overexpressed ROS, and glutathione (GSH) *et al.*, developing TME-responsive inorganic NPs with intrinsic imaging signal and therapeutic function activation can significantly reduce background signal interference (high SNR) and normal tissue toxicity, achieving tumor specific theranostics. Therefore, biodegradation and a "turn-on" theranostic strategy are essential for the future development and clinical transformation of inorganic NPs.

In this review, we summarize the recent advances in the TME-triggered biodegradation of inorganic NPs accompanied by imaging signal amplification and released ions-mediated tumor therapy (Scheme 1). First, the feature characteristics of the TME are introduced, including mild acidity, hypoxia, overexpressed ROS, and glutathione (GSH). Then, the induced biodegradation of NPs in the TME to enhance imaging signals, such as MR imaging and fluorescence imaging is described. Furthermore, tumor therapies, through the generation of toxic ROS by the released ions from mediated "Fenton" and "Fenton-like" reactions and the interference of biological effects in cells, are reviewed. Finally, the challenges and outlook for improving the degradation efficiency, imaging, specificity and efficiency of tumor imaging and treatment are discussed.

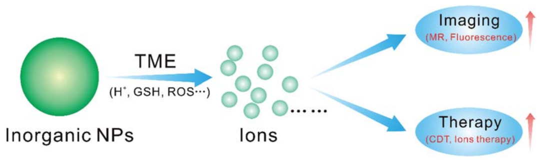

Scheme 1 Schematic illustration showing the tumor microenvironment (H^+, GSH, ROS, *etc.*) triggering the biodegradation of inorganic NPs for enhanced tumor imaging (MR imaging, fluorescence imaging) and therapy (chemodynamic therapy, ions therapy).

2. Feature characteristics of the TME

The tumor microenvironment (TME), which is created by interactions between nontransformed and malignant cells, is a complex physical and biochemical system that plays a crucial role in tumor occurrence, growth, and metastasis.[21,22] Compared with normal tissues, there are many significant differences in the TME, which are listed as follows:

(1) Mild acidity: mild acidity is regarded as one of the most archetypal characteristics of the TME. According to previous inferences, this mild acidity is the result of the accumulation of lactate ($\text{p}K_\text{a} = 3.86$), the metabolite of excessive aerobic glycolysis (Warburg effect).[23] In 2008, Gallagher *et al.*[24] exploited the dynamic nuclear polarization (DNP) technique to realize the *in vivo* MR imaging of tissue pH based on the ratio of hyperpolarized bicarbonate ($H^{13}CO_3^-$) and $^{13}CO_2$ signal intensities after the intravenous injection of hyperpolarized $H^{13}CO_3^-$. After MR imaging of an EL4 tumor pH *in vivo*, they found that the pH value of tumor interstitials was lower than that of the surrounding tissues. According to previous research, the pH value range of the tumor extracellular and intracellular environment is within 6.0–7.0 and 6.0–6.5, respectively.[24]

(2) Overexpressed glutathione (GSH): glutathione (GSH) is the most abundant intracellular cysteine-containing small molecule biothiol. Its role is to maintain the balance of the redox state in the cell and is a vital endogenous antioxidant. The ratio of reduced glutathione (GSH) to its oxidized form (GSSH) is an important indicator of the redox state of the cell and determines the antioxidant capacity of the cell. It has been reported that the GSH level in tumor cells is ~10 mM, which is significantly higher than that in normal cells (~2 μM).[25] Thus, GSH can be used as an endogenous tumor stimulator to achieve reduction-responsive drug release.[26]

(3) Hypoxia: tumor hypoxia is caused by the rapid proliferation of tumor cells, which consumes a large amount of oxygen and decreases oxygen delivery efficiency due to the abnormal structure and function of tumor tissue.[27,28] In some solid tumors, the partial pressure of oxygen is close to 0 mmHg, while the partial pressure of oxygen in normal tissue is 30 mmHg. Furthermore, tumor cells that are farther away from the blood vessel have a lower partial pressure of oxygen, making it difficult to deliver drugs into the tumor tissue. As a result, the treatment efficiency of radiotherapy and chemotherapy on hypoxic cells is weakened.[29] Thus, some conjugated polymers have been designed and synthesized to encapsulate drugs, followed by their release under hypoxic conditions.

(4) H_2O_2: in a previous study, it has been found that tumor cells can produce higher concentrations of H_2O_2 than normal cells.[30,31] H_2O_2 can induce DNA damage and mutations as well as increase genetic instability.[32] At the same time, an increase in H_2O_2 concentration can also activate HIF-1, which plays a role in apoptosis resistance, invasion/metastasis, angiogenesis and immortality.[33] By leveraging the overexpressed H_2O_2 in tumors, some inorganic NPs can be designed to catalyze H_2O_2 to O_2, thus relieving tumor hypoxia. In addition, H_2O_2 can trigger the hydrophilic–hydrophobic transition of some polymers, causing

the drug release in tumors while avoiding side effects in normal tissues.[34,35]

3. TME-triggered biodegradation of NPs for enhanced tumor imaging

3.1. TME-activated MR imaging

As a powerful imaging technique, MR imaging has been widely used in tumor detection due to a series of advantages, such as its high spatial resolution, lack of ionizing radiation, no penetration depth limit, and excellent soft tissue contrast *et al.*[36,37] Currently, most nanoscale MR contrast agents (CAs) have a high relaxivity and exhibit a good contrast effect, improving the accuracy of tumor detection. However, most of these CAs are difficult to degrade, resulting in long-term toxicity. To resolve this problem, during the past few years, biodegradable nanoscale CAs have been developed to amplify by MR signals in tumors.

3.1.1 Mn-based MR CAs. Manganese(II), which has five unpaired electrons and high r_1 relaxivity, is a typical paramagnetic ion that has been widely used for MR imaging.[38] In comparison, Mn^{4+} ions exhibited a lower r_1 relaxivity due to fewer unpaired electrons, thus manganese dioxide (MnO_2) NPs show an insignificant MR contrast effect. Nonetheless, MnO_2 NPs has still attracted research interest in the past decades due to their biodegradability in the TME, yielding Mn^{2+} and improving r_1 relaxivity. For instance, Chen *et al.*[39] found that the r_1 relaxivity of synthesized 2D MnO_2 nanosheets was as low as 0.007 mM^{-1} s^{-1}. However, after an acidic buffer solution treatment (pH = 6.0 and 4.6), the r_1 relaxivity exhibited a significant increase from 0.007 mM^{-1} s^{-1} to 3.4 mM^{-1} s^{-1} and 4.0 mM^{-1} s^{-1}, respectively, due to the emergence of Mn^{2+}. Then, the 2D-MnO_2 nanosheets were employed as ultrasensitive pH-responsive MR CAs for *in vivo* imaging. In addition to MnO_2 NPs, other Mn-doped inorganic NPs have also been developed to explore TME-activated MR imaging. For instance, Mi *et al.*[40]

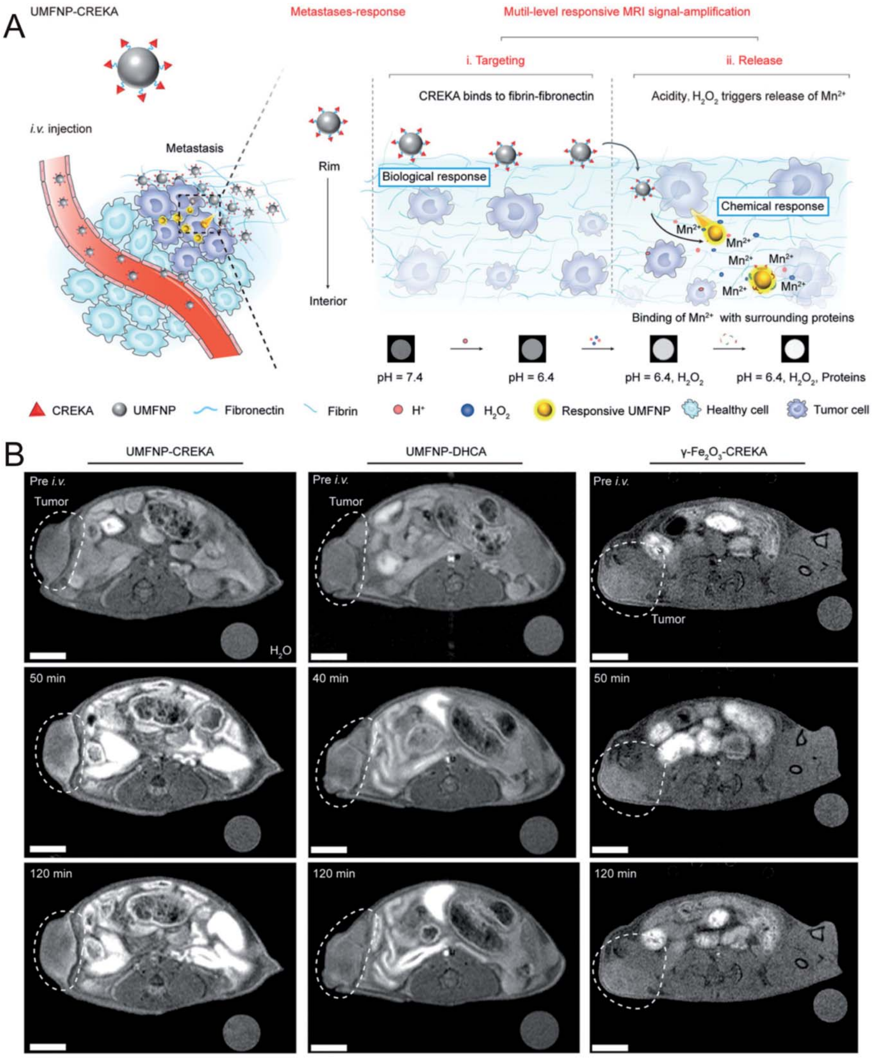

Fig. 1 Schematic illustration showing UMFNP–CREKA NPs as a TME (mild acidity and H_2O_2)-activated T_1-weighted MR imaging probe; (B) *in vivo* time-dependent MR images before and after the intravenous injection of UMFNP–CREKA NPs, UMFNP–DHCA NPs, and γ-Fe_2O_3–CREKA NPs, from left to right, respectively.[43] Copyright from Wiley, 2020.

doped Mn^{2+} into pH-sensitive calcium phosphate (CaP) NPs comprising a poly(ethylene glycol) shell. After intravenous injection and accumulation in the tumor, the low pH of the TME could trigger the disintegration of CaP, resulting in the release of Mn^{2+} ions. Thus, the significant tumor-to-normal (T/N) tissue contrast ratio was significantly increased by approximately 170% for several hours, which is higher than that of clinically used MR CAs (Gd-DTPA, T/N = 120%).

In addition, other Mn-doped inorganic NPs, such as Mn-doped layered double hydroxide (LDHs)[41] and Mn-doped biodegradable SiO_2 (ref. 42) have been reported as pH- or redox-sensitive MR probes for *in vivo* tumor imaging. Very recently, Nie *et al.*[43] synthesized ultrasmall manganese ferrite NPs, followed by modification with a tumor-targeting CREKA (Cys–Arg–Glu–Lys–Ala) peptide to form UMFNP–CREKA NPs. In the presence of mild acidity and H_2O_2, Mn^{2+} was released from UMFNP–CREKA NPs, resulting in a significant increase in the T_1 signal. Moreover, the accumulated Mn^{2+} could bind with proteins in the cancerous tissues, which further improved the T_1 MR signal and brightened the metastatic tumor (Fig. 1A). As displayed in Fig. 1B, the T_1-weighted MR signal of the tumor was significantly enhanced 50 min after the injection of UMFNP–CREKA NPs, while the signals of the other two control groups exhibited a negligible increase. These results demonstrated that the *in vivo* T_1 MR signal was activated by the Mn^{2+} release due to the TME (mild acidity and H_2O_2).

3.1.2 Fe-based MR CAs. Similar to Mn(II), the outer unpaired electrons of Fe(III) make it another magnetic element candidate for designing MR CAs. For example, Fe-based inorganic NPs, such as magnetic iron oxide (>5 nm), are well known T_2-weighted MR CAs, and Fe^{3+}-based metal organic complexes exhibit a remarkable T_1 contrast enhancement effect.[44] However, T_2-weighted MR CAs usually produce dark signals in lesions that are easily disturbed by other hypointense regions such as calcification, air, blood clots, and hemorrhage, while bright signals produced by T_1-weighted MR CAs often interfere with the background signal from normal tissues. Thus, developing tumor-specific T_1-weighted MR imaging probes is of great importance in improving the significant T/N tissue contrast ratio.

In a previous study, Yu *et al.*[46] focused on the synthesis and tumor theranostics of iron carbide NPs (Fe_5C_2). They measured the transverse relaxivity (r_2) of Fe_5C_2 NPs to be 312 mM^{-1} s^{-1}, indicating a remarkable T_2 contrast enhancement effect. To realize tumor-activated MR imaging, in recent work, they fabricated $Fe_5C_2@Fe_3O_4$ NPs with a core–shell structure, which were highly magnetic and demonstrated T_2-weighted MR imaging effects in normal tissue. However, $Fe_5C_2@Fe_3O_4$ NPs show pH sensitivity in acidic environments, accompanied by the release of paramagnetic ferric ions (Fig. 2A). After dispersing the $Fe_5C_2@Fe_3O_4$ NPs in acidic phosphate-buffered saline (PBS) (pH = 5.4), the transverse relaxation rate (r_2) was reduced from 203.83 mM^{-1} s^{-1} to 64.18 mM^{-1} s^{-1}, while the longitudinal relaxation rate (r_1) was increased from 0.26 mM^{-1} s^{-1} to 1.01 mM^{-1} s^{-1} (Fig. 2B). Thus, after 24 h of intravenous injection, the T_1-weighted MR signal in the tumor was significantly enhanced from 99.1% to 123.7%, successfully achieving an acidic tumor environment-activated MR imaging enhancement (Fig. 2C).[45]

3.2. TME-activated fluorescence imaging

Compared with MR imaging, the most significant advantage of fluorescence imaging is its high sensitivity. To date, a series of

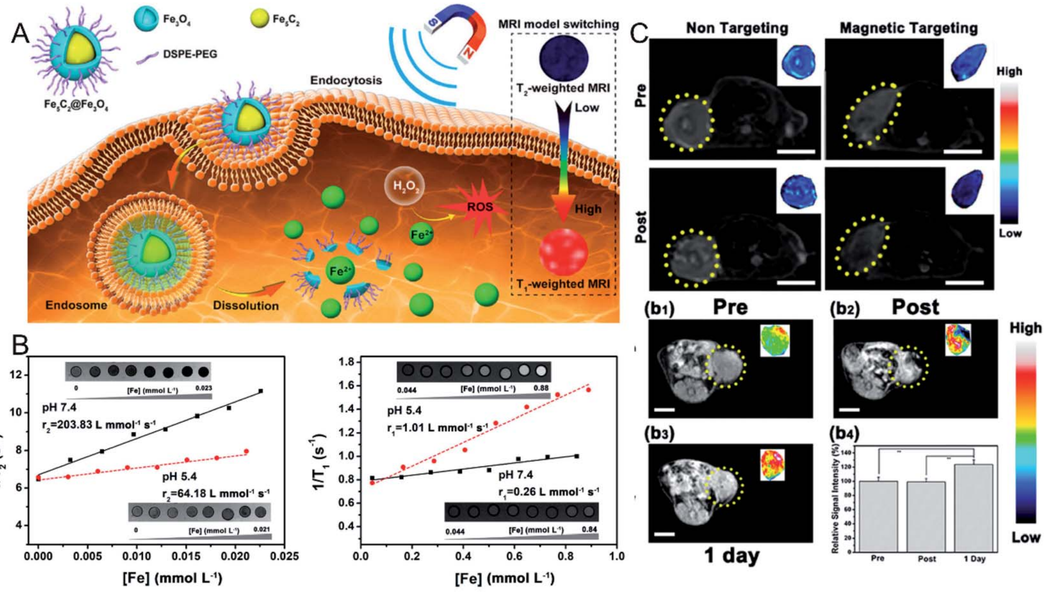

Fig. 2 (A) Schematic illustration showing the $Fe_5C_2@Fe_3O_4$ NPs as a TME-activated T_1-weighted MR imaging probe. (B) The *in vitro* MR images, transverse and longitudinal relaxation rates of $Fe_5C_2@Fe_3O_4$ NPs in different pH conditions (7.4 and 5.5); (C) *in vivo* T_2-weighted MR images before and after the intravenous injection of $Fe_5C_2@Fe_3O_4$ NPs with and without magnetic targeting; *in vivo* T_1-weighted MR images before and after the intratumoral injection of $Fe_5C_2@Fe_3O_4$ NPs, and the relative signal intensities.[45] Copyright from American Chemical Society, 2019.

materials with excellent fluorescence properties have been developed, including organic dyes, quantum dots (QDs), metal nanoclusters, and upconversion NPs (UCNPs) *et al.* However, the greatest obstacle to *in vivo* fluorescence imaging is autofluorescence interference from tissues. Thus, a "turn-on" strategy is usually designed to specifically activate the fluorescence signal at the tumor site and achieve low background fluorescence during imaging. For instance, manganese dioxide (MnO_2)NPs, a classic biodegradable material in the TME, have been widely used as a surface modification of fluorescence probes. As a result, the fluorescence signal is quenched due to the fluorescent resonance energy transfer (FRET) effect that occurs between the MnO_2 and fluorescent probes. Thus, after intravenous injection, no fluorescence signal can be detected in normal tissues and organs. However, after accumulation in the tumor, the MnO_2 NPs modified on the surface of the probe can be decomposed by GSH, H_2O_2, and the acidic TME, resulting in the recovery of the fluorescence signal of the probe and realizing tumor-specific fluorescence imaging. For instance, Kong *et al.*[47] synthesized silicon quantum dots (Si QDs), followed by conjugation with photosensitizer (Ce6) and MnO_2 nanoparticles, respectively. As a result, the obtained BSA–Ce6–Si–MnO_2 nanoparticles exhibited weak fluorescence due to FRET effect induced by MnO_2. After entering into tumor cells, the fluorescence signal of Si QDs and Ce6 were recovered due to MnO_2 degradation in the presence of acid condition and H_2O_2, realizing tumor specific fluorescence imaging. To further increase light penetration and reduce background signal interference, Liu *et al.*[48] constructed UCNP–MnO_2 FRET nanosystem using a similar strategy, which was applied for GSH detection.

In addition, Yang *et al.*[49] reported another strategy to realize TME-activated fluorescence imaging by assembling a disulfide-bond-linked hydroxyethyl starch paclitaxel (HES–SS–PTX) conjugate and a near-infrared (NIR) cyanine fluorophore DiR. First, the fluorescence signal was quenched due to the aggregation-caused quenching (ACQ) effect. However, after the NPs were internalized by tumor cells, the disulfide bond (S–S) of HES–SS–PTX could be cleaved by intracellular GSH, resulting in the synchronized release of conjugated PTX and loaded DiR. The released DiR dyes restored the fluorescent properties of the NPs. Two hours after the injection, the fluorescence signal was detected at the tumor site, and the signal of nanoparticles was significantly higher than that of free DiR dyes.

4. TME-triggered biodegradation of nanoparticles for enhanced tumor therapy

4.1. Tumor chemodynamic therapy (CDT)

Traditional cancer treatment strategies such as surgical resection, chemotherapy and radiotherapy have obvious side effects. Emerging phototherapy strategies, such as photodynamic therapy and photothermal therapy, are often limited by the penetration depth of light. Therefore, developing an efficient and safe treatment strategy is particularly important.

The Fenton reaction, a classic inorganic chemical reaction, is a process in which Fe^{2+} ions catalyze the decomposition of hydrogen peroxide (H_2O_2) to produce hydroxyl radicals ($\cdot$OH), which are widely used in wastewater treatment due to their effectiveness in removing refractory organic pollutants. In the past few years, because $\cdot$OH can induce protein denaturation, DNA breakage, phospholipid membrane damage, and mitochondrial destruction of tumor cells, the Fenton reaction has begun to be turned toward tumor therapy, which was named as tumor chemodynamic therapy.

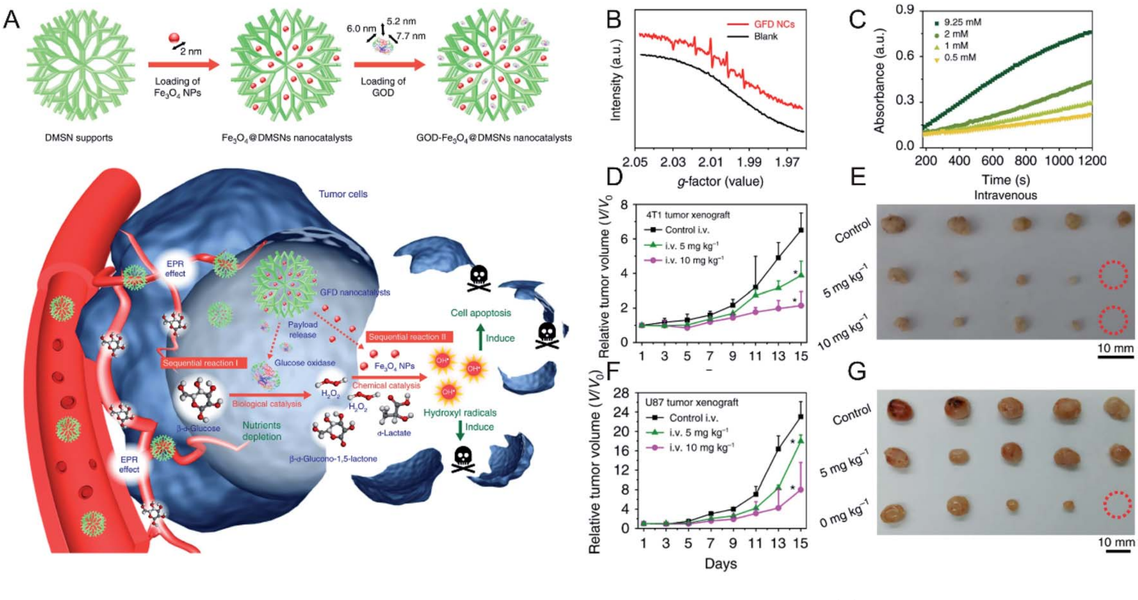

Fig. 3 (A) Schematic illustration showing GOD–Fe_3O_4@DMSN for tumor selective catalytic therapy. (B) ESR spectra of GOD–Fe_3O_4@DMSN with and without the addition of glucose oxidase; (C) time-dependent absorbance of TMB with different concentrations of glucose oxidase; tumor growth curves and tumor images of (D and E) 4T1 and (F and G) U87 tumor-bearing mice.[50] Copyright from Springer Nature, 2017.

4.1.1 Fe ions-mediated tumor chemodynamic therapy. Superparamagnetic iron oxide NPs (SPIONs) have been broadly explored in versatile biomedical applications, including magnetic hyperthermia, magnetic-targeted drug delivery, and MR imaging. In addition, the SPIONs-mediated Fenton reaction has been explored in tumor therapy applications. For instance, Huo *et al.*[50] synthesized biodegradable dendritic silica NPs with large pore (~40 nm), followed by loading ultrasmall Fe_3O_4 NPs (~2 nm) and glucose oxidase (6.0 nm × 5.2 nm × 7.7 nm) (Fig. 3A). After the intravenous injection and accumulation of the above NPs in tumors, glucose oxidase could decrease the amount of glucose in tumor cells and provide sufficient H_2O_2 for the subsequent Fenton reaction that was mediated by Fe ions derived from the degradation of the Fe_3O_4 NPs in the mildly acidic TME. Both electron spin resonance (ESR) measurements (Fig. 3B) and 3,3′,5,5′-tetramethylbenzidine (TMB) absorption spectra (Fig. 3C) confirmed the generation of ·OH. As displayed in Fig. 3D–G, the produced ·OH significantly inhibited the growth of 4T1 tumors (Fig. 3D and E) and U87 glioblastoma tumors (Fig. 3F and G) without obvious side effects. In addition to SPIONs, other Fe-based NPs have been developed for the combination of CDT and other treatment strategies. For instance, Hu *et al.*[51] designed a NO-associated CDT system by mixing Fe^{3+} and coordination polymers (1, 5-bis[(L-proline-1-yl)diazen-1-ium-1, 2-diol O^2-yl]-2,4-dinitrobenzene BPDB, NO donor), followed by ion exchange, forming Fe(II)-BNCP NPs. Subsequently, it was found that Fe(II)-BNCP could both efficiently catalyze H_2O_2 to produce ·OH and generate NO in the presence of GSH. Thus, tumor growth of the group treated with Fe(II)-BNCP was significantly suppressed compared with other control groups. This work not only demonstrated the great promise of gas therapy-CDT-enhanced antitumor activity but also provided a novel strategy to design prodrug-based nanoplatform with high drug loading efficiency for precise tumor treatment. Chen *et al.*[52] prepared $CuFeS_2$ NPs by using a protein biomimetic strategy. The $CuFeS_2$ NPs exhibited not only a significant ability to produce ·OH but also high photothermal conversion efficacy. Consequently, tumor growth was efficiently inhibited by the combined CDT-photothermal therapy. Thus, combination of CDT and other treatment strategies will be promising for cancer therapy.

4.1.2 Cu ions-mediated tumor chemodynamic therapy. Although the Fe^{2+}-mediated Fention reaction has been developed as a safe strategy for cancer therapy, the reaction efficiency is high only in strongly acidic conditions (pH = 2–4).[53] Thus, the production of ·OH is limited in weakly acidic tumor environments (pH = 5.5–6.5). In contrast, it has been reported that the reaction rate of Cu^+-catalyzed Fenton-like reactions is as high as $1 \times 10^4\ M^{-1}\ s^{-1}$ under weakly acidic and neutral

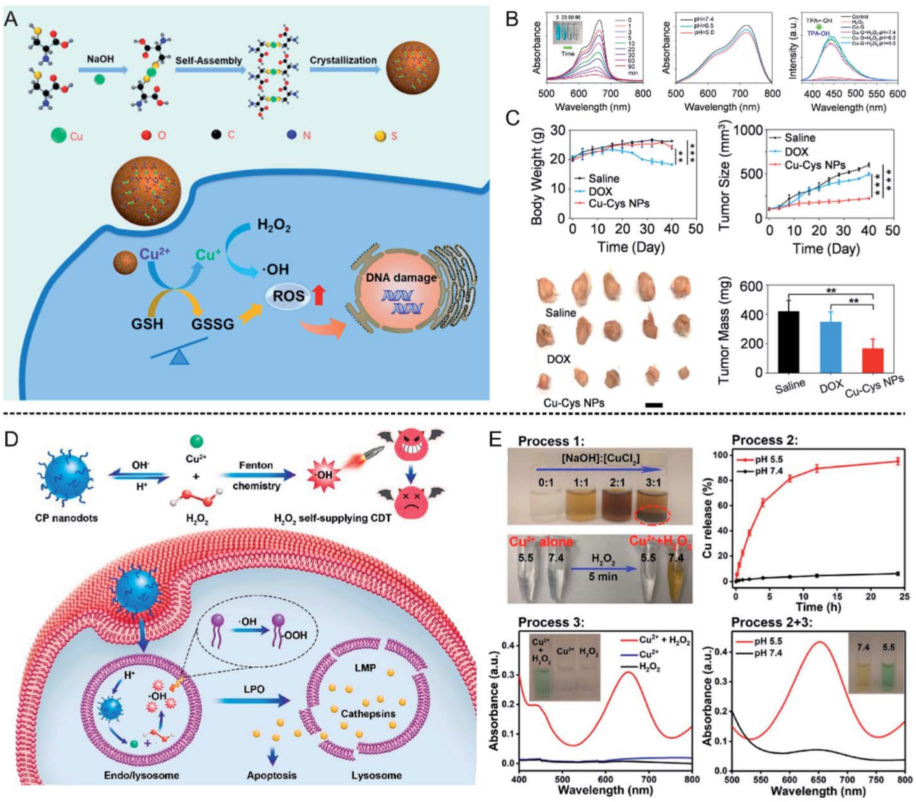

Fig. 4 (A) Schematic illustration showing Cu–Cys NPs for tumor chemodynamic therapy; (B) characterization of hydroxyl radical (·OH) generation; (C) body weight, tumor size, tumor image, and tumor mass of different treatment groups (saline injection, DOX injection, and Cu–Cys NPs injection).[56] Copyright from American Chemical Society, 2019. (D) Schematic illustration showing copper peroxide (CP) nanodots for self-supplying H_2O_2-enhanced chemodynamic therapy of tumors; (E) characterization of hydroxyl radical (·OH) generation in different pH conditions (5.5 and 7.4).[57] Copyright from American Chemical Society, 2019.

conditions, which is a ~160-fold increase over that of Fe^{2+}-catalyzed Fenton reactions.[54,55] For instance, Li *et al.*[56] synthesized copper–cysteine NPs (Cu–Cys NPs) that depended on the high coordination interaction between the sulfhydryl group (–SH) and Cu ions. After entering the cell by endocytosis, the Cu^{2+} in the Cu–Cys NPs could be reduced to Cu^{+} by GSH, followed by catalyzing H_2O_2 to trigger the Fenton-like reaction (Fig. 4A). As shown in Fig. 4B, the absorption peak of methylene blue (MB) exhibited a time-dependent downward trend, indicating the gradual generation of ·OH. More importantly, the reaction rate differs by only 10% under different pH conditions (pH = 5.5, 6.4, and 7.4), which ensured the high efficiency of the Cu–Cys NP-mediated CDT therapy of tumors. It can be seen from the tumor growth curve and tumor images (Fig. 4C) that the CDT efficiency was significantly higher than that of conventional chemotherapy (DOX-injection group). Thus, it can be seen the efficiency of Cu ions-mediated Fenton reaction is higher than Fe ions, which will be more effective for tumor therapy.

Furthermore, the content of H_2O_2 is a crucial factor affecting the efficiency of the Fenton reaction. Therefore, to further increase the H_2O_2 concentration at the tumor site, Lin *et al.*[57] synthesized copper peroxide (CP) nanodots by a coordination of Cu^{2+} and H_2O_2 in the presence of hydroxide ions (OH^{-}), which could realize a self-supply of H_2O_2 at an acidic pH for enhanced CDT (Fig. 4D). Under acidic conditions, CP nanodots could release Cu^{2+} as well as H_2O_2, thus ·OH was produced, which was confirmed by using TMB as an indicator (Fig. 4E). The synthesized CP nanodots are the first example of a Fenton-type metal peroxide NPs, which provides new guidance for the development of other peroxides to enhance the CDT of tumors. In addition, Cu ion-mediated CDT can also be combined with other treatment strategies to enhance tumor therapy. Copper sulfide (CuS) is a common photothermal agent, and the application of CuS for tumor photothermal therapy has been systematically studied. Wu *et al.*[58] found that the fabricated ultrasmall Cu_{2-x} S-PEG nanodots could catalyze H_2O_2 into ·OH, and this reaction could be enhanced under laser irradiation at 1064 nm due to the heat generated by the Cu_{2-x} S-PEG photothermal agent. Consequently, the combination of photothermal therapy (PTT) and CDT significantly suppressed tumor growth 2 days after treatment, and the tumors disappeared after 14 days, indicating good combined treatment efficiency.

4.1.3 Other ions-mediated tumor chemodynamic therapy.

In addition to Fe and Cu ions, other metal ions, such as Co, Mn, and Ti ion-mediated Fenton-like reactions for CDT of tumors have been reported in recent years. Liang *et al.*[59] synthesized CaO_2 NPs, followed by loading DOX and adding Co^{2+} and 2-methylimidazole to forme CaO_2@DOX@ZIF-67 NPs. In this work, ZiF-67 could be degraded under acidic conditions (pH = 5.0), leading to the release of Co^{2+} and triggering the Fenton-like reaction. More importantly, H_2O_2 could be efficiently self-supplied through the reaction between CaO_2 and H_2O to enhance the production of ·OH. Moreover, DOX could also be released in the TME, achieving a combined chemo/chemodynamic treatment of tumors. In addition to increasing the H_2O_2 concentration, reducing the GSH level is another strategy to ensure the generation of ·OH rather than being removed by overexpressed GSH in tumor cells. Lin *et al.*[60] first reported a MnO_2 CDT agent that could deplete GSH through a reaction and degrade into Mn^{2+}. Subsequently, they found that H_2O_2 could be catalyzed by Mn^{2+} into ·OH in the presence of HCO_3^{-1}. The activated MR signals guided the CDT of tumor. TiO_2 is a well-known sonosensitizer for sonodynamic therapy (SDT) of tumors. Very recently, Cheng *et al.*[61] reported that Ti^{3+} is another alternative to iron ions for Fenton-like reactions. First, they synthesized ultrathin titanium monoxide (TiO_{1+x}) nanorods and found that the ROS productivity under ultrasonic excitation was significantly higher than that of common TiO_2 NPs. More importantly, the Ti ion-mediated Fenton-like reaction could be dramatically enhanced by ultrasonic excitation, achieving a combination of SDT and ultrasound-enhanced CDT of tumors. Thus, in our opinion, other metal elements with variable valence can be considered to be used for tumor therapy through Fenton reaction.

4.2. Ions interference therapy (IIT)

Unlike the above metal ions that generate ROS through the Fenton reaction to kill tumor cells (Table 1), ion interference therapy is a new tumor treatment strategy that induces cell apoptosis by blocking the biological effects and functions of cells, which was first reported in last year. Inspired by the

Table 1 Comparison between chemodynamic therapy (CDT) and ions interference therapy (IIT)

	Ions	Conditions	Mechanism of tumor therapy	Advantages	Disadvantages	Ref.
CDT	Fe^{2+}	H_2O_2, H^+	Ions catalyze the decomposition of H_2O_2 to produce ·OH through fenton reaction, inducing protein denaturation, DNA breakage, and mitochondrial destruction of tumor cells	Safe, specific tumor therapy without side effects	The efficiency is limited by amount of H_2O_2	50–52
	Cu^{+}	H_2O_2, H^+				15,56 and 57
	Mn^{2+}	H_2O_2, H^+, HCO_3^{-}				60
	Co^{2+}	H_2O_2, H^+				59,62
IIT	Ca^{2+}	—	Inducing cell apoptosis by blocking the biological effects and functions of tumor cells	Safe, high efficiency, specific tumor therapy without side effects	The efficiency is constrained by the self-regulatory function of the cell and requires combination with other strategies	63,64

emergence of microcalcifications in tumors after radiotherapy or chemotherapy (Fig. 5A), Zhang *et al.*[63] synthesized ultrasmall CaO_2 NPs (~5 nm, Fig. 5B), followed by coating a sodium hyaluronate layer on their surface to obtain SH-CaO_2 NPs. In the tumor lesion area, the protective layer was decomposed by overexpressed hyaluronidase, thus the exposed CaO_2 NPs were accelerated to decompose in the acidic TME, producing H_2O_2 and free Ca^{2+}. Due to the downregulation of catalase expression in tumor cells, H_2O_2 accumulated in the tumor cells and induced oxidative stress, which further led to the dysfunction of Ca-related ion channels. Thus, the Ca^{2+} concentration in tumor cells was unable to be regulated, resulting in the long-term retention of Ca. Over time, the abnormal Ca^{2+} aggregation triggered persistent calcium overload, hindered the metabolism of tumor cells, and induced metabolic disorders and functional dysfunction of tumor cells, thereby inducing cell death. At the same time, the local increase in Ca^{2+} concentration could also promote the development of microcalcifications in tumor lesions. This type of tumor cell death, which is induced by ultrasmall calcium peroxide NPs, is defined as "calcium death". As displayed in CT images of tumors before and after injection (Fig. 5C), the CT signal is slightly enhanced 3 h after injection, but becomes significantly brighter after 3 days, indicating the existence of tumor calcification. Correspondingly, tumor growth is inhibited 14 days after treatment.

Furthermore, Ca^{2+}-mediated ion interference therapy can be combined with other treatment strategies. Recently, Liu *et al.*[64] synthesized hollow $CaCO_3$ NPs, followed by loading an inhibitor for GSH biosynthesis (L-buthionine sulfoximine, BSO) and a sonosensitizer (meso-tetra-(4-carboxyphenyl) porphine, TCPP). As shown in Fig. 5E, the $CaCO_3$ NPs were degraded under acidic conditions, and the released Ca^{2+} ions overloaded the tumor cells and induced mitochondrial damage. Moreover, the TCPP sonosensitizer was able to produce ROS under ultrasonic excitation, and the released BSO ensured that the ROS could not be removed by GSH. Eventually, the triple amplification of tumor oxidative stresses was applied toward tumor therapy. As displayed in Fig. 5F and G, the tumors of mice treated with BSO-TCPP/Fe^{3+}@$CaCO_3$ NPs and ultrasonication showed extremely slow growth compared with other groups, and the corresponding tumor inhibition rates were 70% (intravenous injection) and 80% (intratumoral injection), respectively. Besides Ca^{2+}, other ions should be explored for their effect on the biological effects of tumor cells and then attempted for tumor therapy.

5. Summary and outlook

In conclusion, we have summarized recent achievements in the biodegradable inorganic NPs for enhanced tumor theranostics, including MR imaging, fluorescence imaging, chemodynamic therapy, and ion interference therapy of tumors. Regarding tumor imaging, the degradation of NPs and subsequent release of metal ions can activate signal, realizing low/no background tumor imaging; regarding tumor therapy, the released metal ions in the TME can produce ROS through the Fenton reaction or block the biological effects and functions of cells to inhibit tumor growth without side effects in normal tissues. Moreover, the degradation of NPs can accelerate their metabolism in the body, avoiding the toxicity from long-term accumulation. We believe that this review paper can guide researchers to find and design these degradable inorganic nanoparticles for tumor theranostics, which is very promising for clinical transformation.

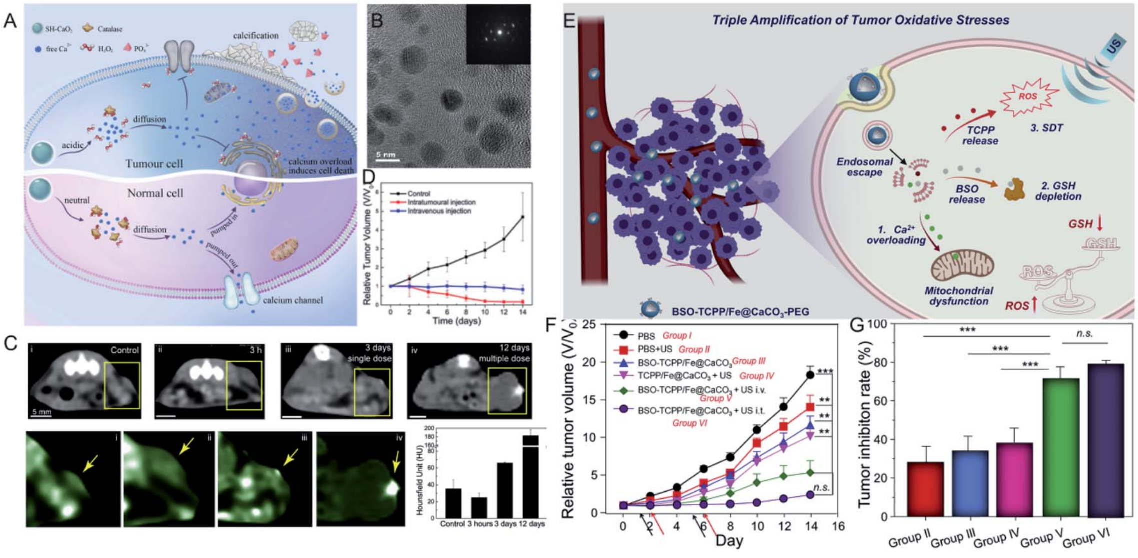

Fig. 5 (A) Schematic illustration showing SH-CaO_2 NPs for Ca^{2+} ion interference therapy of tumors; (B) TEM image of SH-CaO_2 NPs; (C) *in vivo* time-dependent CT images of tumors before and after SH-CaO_2 NPs injection; (D) tumor growth curve of the control group, the intratumoral injection of SH-CaO_2 NPs, and the intravenous injection of SH-CaO_2 NPs;[63] copyright from Elsevier, 2019. (E) Schematic illustration showing BSO-TCPP/Fe@$CaCO_3$-PEG NPs for the triple amplification of tumor oxidative stresses and tumor therapy; (F) tumor growth curve and tumor inhibition rate of different treatment groups.[64] Copyright from Elsevier, 2020.

Despite substantial progress made by many groups in designing biodegradable inorganic NPs for tumor imaging and therapy, it is fair to admit that there are still many problems that need to be addressed in the future: (1) the *in vivo* potential toxicity induced by released metal ions after degradation should be considered, as those metal ions can easily bind to proteins or enzymes. (2) The degradation of inorganic NPs is too monotonous and needs to be expanded. Currently, acidic conditions are predominant in decomposing inorganic NPs, but the degradation efficiency is not sufficient. Therefore, according to the characteristics of the TME (pH, GSH, hypoxia, H_2O_2, and enzymes), designing NPs that respond to multiple triggers is very effective in accelerating degradation. (3) After degradation, the efficacy of metal ion-mediated tumor treatment is still not efficient, especially in terms of the tumor inhibitory rate. Therefore, the earlier diagnosis and treatment of tumors combined with other strategies are particularly necessary. In essence, great effort should be devoted to resolving the *in vivo* degradation efficiency of inorganic NPs and enhancing tumor theranostics.

Conflicts of interest

There are no conflicts to declare.

Acknowledgements

This research was funded by National Nature Science Foundation of China (NSFC, 81801823), State Key Laboratory of Molecular Engineering of Polymers (Fudan University, K2020-16), and Shanghai Sailing Program (19YF1450700).

References

1 C. Allemani, T. Matsuda, V. Di Carlo, R. Harewood, M. Matz, M. Nikšić, A. Bonaventure, M. Valkov, C. J. Johnson and J. Estève, *Lancet*, 2018, **391**, 1023–1075.
2 L. A. Torre, F. Bray, R. L. Siegel, J. Ferlay, J. Lortet-Tieulent and A. Jemal, *Ca-Cancer J. Clin.*, 2015, **65**, 87–108.
3 A. Yahia-Ammar, D. Sierra, F. Mérola, N. Hildebrandt and X. Le Guével, *ACS Nano*, 2016, **10**, 2591–2599.
4 M. N. Rhyner, A. M. Smith, X. Gao, H. Mao, L. Yang and S. Nie, *Nanomedicine*, 2006, **1**, 209–217.
5 A. Gautam and P. Komal, *Coord. Chem. Rev.*, 2018, **376**, 393–404.
6 S.-K. Sun, H.-F. Wang and X.-P. Yan, *Acc. Chem. Res.*, 2018, **51**, 1131–1143.
7 T. Maldiney, A. Bessière, J. Seguin, E. Teston, S. K. Sharma, B. Viana, A. J. Bos, P. Dorenbos, M. Bessodes and D. Gourier, *Nat. Mater.*, 2014, **13**, 418–426.
8 M. Wu, Y. Xue, N. Li, H. Zhao, B. Lei, M. Wang, J. Wang, M. Luo, C. Zhang and Y. Du, *Angew. Chem., Int. Ed.*, 2019, **58**, 6880–6885.
9 P. Li, P. Chevallier, P. Ramrup, D. Biswas, D. Vuckovich, M.-A. Fortin and J. K. Oh, *Chem. Mater.*, 2015, **27**, 7100–7109.
10 F. Ratto, S. Centi, C. Avigo, C. Borri, F. Tatini, L. Cavigli, C. Kusmic, B. Lelli, S. Lai and S. Colagrande, *Adv. Funct. Mater.*, 2016, **26**, 7178–7185.
11 R. Meir, K. Shamalov, O. Betzer, M. Motiei, M. Horovitz-Fried, R. Yehuda, A. Popovtzer, R. Popovtzer and C. J. Cohen, *ACS Nano*, 2015, **9**, 6363–6372.
12 K. Cherukula, K. Manickavasagam Lekshmi, S. Uthaman, K. Cho, C.-S. Cho and I.-K. Park, *Nanomaterials*, 2016, **6**, 76.
13 X. Yi, K. Yang, C. Liang, X. Zhong, P. Ning, G. Song, D. Wang, C. Ge, C. Chen and Z. Chai, *Adv. Funct. Mater.*, 2015, **25**, 4689–4699.
14 V. Deepagan, D. G. You, W. Um, H. Ko, S. Kwon, K. Y. Choi, G.-R. Yi, J. Y. Lee, D. S. Lee and K. Kim, *Nano Lett.*, 2016, **16**, 6257–6264.
15 X. Zhong, X. Wang, L. Cheng, Y. a. Tang, G. Zhan, F. Gong, R. Zhang, J. Hu, Z. Liu and X. Yang, *Adv. Funct. Mater.*, 2019, 1907954.
16 P. Liu, W. Yang, L. Shi, H. Zhang, Y. Xu, P. Wang, G. Zhang, W. R. Chen, B. Zhang and X. Wang, *J. Mater. Chem. B*, 2019, **7**, 6924–6933.
17 W. Yang, W. Guo, W. Le, G. Lv, F. Zhang, L. Shi, X. Wang, J. Wang, S. Wang and J. Chang, *ACS Nano*, 2016, **10**, 10245–10257.
18 E. B. Ehlerding, F. Chen and W. Cai, *Adv. Sci.*, 2016, **3**, 1500223.
19 D. Reichel, M. Tripathi, P. Butte, R. Saouaf and J. M. Perez, *Nanotheranostics*, 2019, **3**, 196.
20 J. Zhang, L. Ning, J. Huang, C. Zhang and K. Pu, *Chem. Sci.*, 2020, **11**, 618–630.
21 Z. Zhou and Z.-R. Lu, *Adv. Drug Delivery Rev.*, 2017, **113**, 24–48.
22 F. R. Balkwill, M. Capasso and T. Hagemann, *J. Cell Sci.*, 2012, **125**, 5591–5596.
23 H. Wu, Z. Ding, D. Hu, F. Sun, C. Dai, J. Xie and X. Hu, *J. Pathol.*, 2012, **227**, 189–199.
24 F. A. Gallagher, M. I. Kettunen, S. E. Day, D.-E. Hu, J. H. Ardenkjær-Larsen, P. R. Jensen, M. Karlsson, K. Golman, M. H. Lerche and K. M. Brindle, *Nature*, 2008, **453**, 940–943.
25 Y. Li, K. Xiao, J. Luo, W. Xiao, J. Lee and K. S. Lam, *Cancer Res.*, 2011, **71**(8), DOI: 10.1158/1538-7445.AM2011-4439.
26 X.-D. Xu, Y.-J. Cheng, J. Wu, H. Cheng, S.-X. Cheng, R.-X. Zhuo and X.-Z. Zhang, *Biomaterials*, 2016, **76**, 238–249.
27 J. Pouysségur, F. Dayan and N. M. Mazure, *Nature*, 2006, **441**, 437–443.
28 D. M. Gilkes, G. L. Semenza and D. Wirtz, *Nat. Rev. Cancer*, 2014, **14**, 430–439.
29 M. R. Horsman, L. S. Mortensen, J. B. Petersen, M. Busk and J. Overgaard, *Nat. Rev. Clin. Oncol.*, 2012, **9**, 674.
30 T. P. Szatrowski and C. F. Nathan, *Cancer Res.*, 1991, **51**, 794–798.
31 C. M. Doskey, V. Buranasudja, B. A. Wagner, J. G. Wilkes, J. Du, J. J. Cullen and G. R. Buettner, *Redox Biol.*, 2016, **10**, 274–284.
32 S. Park, X. You and J. A. Imlay, *Proc. Natl. Acad. Sci. U. S. A.*, 2005, **102**, 9317–9322.
33 G. L. Semenza, *Nat. Rev. Cancer*, 2003, **3**, 721–732.

34 Y. Kuang, K. Baakrishnan, V. Gandhi and X. Peng, *J. Am. Chem. Soc.*, 2011, **133**, 19278–19281.
35 S. Park, J. Yoon, S. Bae, M. Park, C. Kang, Q. Ke, D. Lee and P. M. Kang, *Biomaterials*, 2014, **35**, 5944–5953.
36 G. Angelovski, *Angew. Chem., Int. Ed.*, 2016, **55**, 7038–7046.
37 D. Ni, W. Bu, E. B. Ehlerding, W. Cai and J. Shi, *Chem. Soc. Rev.*, 2017, **46**, 7438–7468.
38 B. Ding, P. Zheng, P. a. Ma and J. Lin, *Adv. Mater.*, 2020, **32**, 1905823.
39 Y. Chen, D. Ye, M. Wu, H. Chen, L. Zhang, J. Shi and L. Wang, *Adv. Mater.*, 2014, **26**, 7019–7026.
40 P. Mi, D. Kokuryo, H. Cabral, H. Wu, Y. Terada, T. Saga, I. Aoki, N. Nishiyama and K. Kataoka, *Nat. Nanotechnol.*, 2016, **11**, 724.
41 B. Li, Z. Gu, N. Kurniawan, W. Chen and Z. P. Xu, *Adv. Mater.*, 2017, **29**, 1700373.
42 L. Yu, Y. Chen, M. Wu, X. Cai, H. Yao, L. Zhang, H. Chen and J. Shi, *J. Am. Chem. Soc.*, 2016, **138**, 9881–9894.
43 Y. Li, X. Zhao, X. Liu, K. Cheng, X. Han, Y. Zhang, H. Min, G. Liu, J. Xu, J. Shi, H. Qin, H. Fan, L. Ren and G. Nie, *Adv. Mater.*, 2020, **32**, 1906799.
44 F. Liu, X. He, H. Chen, J. Zhang, H. Zhang and Z. Wang, *Nat. Commun.*, 2015, **6**, 8003.
45 J. Yu, F. Zhao, W. Gao, X. Yang, Y. Ju, L. Zhao, W. Guo, J. Xie, X.-j. Liang and X. Tao, *ACS Nano*, 2019, **13**, 10002–10014.
46 J. Yu, C. Yang, J. Li, Y. Ding, L. Zhang, M. Z. Yousaf, J. Lin, R. Pang, L. Wei and L. Xu, *Adv. Mater.*, 2014, **26**, 4114–4120.
47 R. Wang, M. Zhao, D. Deng, X. Ye, F. Zhang, H. Chen and J. Kong, *J. Mater. Chem. B*, 2018, **6**, 4592–4601.
48 R. Deng, X. Xie, M. Vendrell, Y.-T. Chang and X. Liu, *J. Am. Chem. Soc.*, 2011, **133**, 20168–20171.
49 Y. Li, Y. Wu, J. Chen, J. Wan, C. Xiao, J. Guan, X. Song, S. Li, M. Zhang, H. Cui, T. Li, X. Yang, Z. Li and X. Yang, *Nano Lett.*, 2019, **19**, 5806–5817.
50 M. Huo, L. Wang, Y. Chen and J. Shi, *Nat. Commun.*, 2017, **8**, 1–12.
51 Y. Hu, T. Lv, Y. Ma, J. Xu, Y. Zhang, Y. Hou, Z. Huang and Y. Ding, *Nano Lett.*, 2019, **19**, 2731–2738.
52 Q. Chen, Y. Luo, W. Du, Z. Liu, S. Zhang, J. Yang, H. Yao, T. Liu, M. Ma and H. Chen, *ACS Appl. Mater. Interfaces*, 2019, **11**, 18133–18144.
53 H. Zhao, Y. Wang, Y. Wang, T. Cao and G. Zhao, *Appl. Catal., B*, 2012, **125**, 120–127.
54 E. Brillas, M. A. Baños, S. Camps, C. Arias, P.-L. Cabot, J. A. Garrido and R. M. Rodríguez, *New J. Chem.*, 2004, **28**, 314–322.
55 T. Soltani and B.-K. Lee, *Chem. Eng. J.*, 2017, **313**, 1258–1268.
56 B. Ma, S. Wang, F. Liu, S. Zhang, J. Duan, Z. Li, Y. Kong, Y. Sang, H. Liu and W. Bu, *J. Am. Chem. Soc.*, 2018, **141**, 849–857.
57 L.-S. Lin, T. Huang, J. Song, X.-Y. Ou, Z. Wang, H. Deng, R. Tian, Y. Liu, J.-F. Wang and Y. Liu, *J. Am. Chem. Soc.*, 2019, **141**, 9937–9945.
58 R. Hu, Y. Fang, M. Huo, H. Yao, C. Wang, Y. Chen and R. Wu, *Biomaterials*, 2019, **206**, 101–114.
59 S. Gao, Y. Jin, K. Ge, Z. Li, H. Liu, X. Dai, Y. Zhang, S. Chen, X. Liang and J. Zhang, *Adv. Sci.*, 2019, **6**, 1902137.
60 L. S. Lin, J. Song, L. Song, K. Ke, Y. Liu, Z. Zhou, Z. Shen, J. Li, Z. Yang and W. Tang, *Angew. Chem., Int. Ed.*, 2018, **57**, 4902–4906.
61 X. Wang, X. Zhong, L. Bai, J. Xu, F. Gong, Z. Dong, Z. Yang, Z. Zeng, Z. Liu and L. Cheng, *J. Am. Chem. Soc.*, 2020, **142**, 6527–6537.
62 Y. Sang, F. Cao, W. Li, L. Zhang and X. Qu, *J. Am. Chem. Soc.*, 2020, **142**, 5177–5183.
63 M. Zhang, R. Song, Y. Liu, Z. Yi, X. Meng, J. Zhang, Z. Tang, Z. Yao, Y. Liu and X. Liu, *Chem*, 2019, **5**, 2171–2182.
64 Z. Dong, L. Feng, Y. Hao, Q. Li, M. Chen, Z. Yang, H. Zhao and Z. Liu, *Chem*, 2020, **6**, 1391–1407.